



Article

# Synthesis and Characterization of Novel $Ti_3SiC_2$ Reinforced Ni-Matrix Multilayered Composite-Based Solid Lubricants

Quan Tran, Matt Fuka, Maharshi Dey and Surojit Gupta \*

Department of Mechanical Engineering, University of North Dakota, Grand Forks, ND 58201, USA; quan.tran@ndus.edu (Q.T.); mattfuka@gmail.com (M.F.); maharshi.dey@und.edu (M.D.)

\* Correspondence: surojit.gupta@engr.und.edu

Received: 13 August 2019; Accepted: 4 December 2019; Published: 9 December 2019



**Abstract:** We report the synthesis and characterization of two different types of Ni-based laminated composites (Types I and II). In Type-I composites, layers of Ni and  $Ti_3SiC_2$  (Ni- $Ti_3SiC_2$ ) were interleaved with Ni, whereas in Type-II composites, Ni- $Ti_3SiC_2$  layers were interleaved with Al and Ni. The laminate thickness and  $Ti_3SiC_2$  content in the individual Ni- $Ti_3SiC_2$  layers were systematically varied in both the composites. Detailed SEM studies showed that  $Ti_3SiC_2$  particulates are well distributed in the Ni-matrix with little or no interfacial reactions with interparticle porosity. However, there were interfacial reactions between Ni and Al in Type II composites. In general, Type I multilayered composites had higher ultimate compressive strength (UCS) in parallel orientation as compared to perpendicular orientation (layers are aligned parallel or perpendicular to the wear surface then it will be referred to as parallel or perpendicular orientation). Comparatively, in Type II composites, the UCS was greater in perpendicular orientation as compared to parallel due to the presence of Al layers as bonding layers. Both the composite designs showed triboactive behavior against alumina disks and sensitivity to laminate thickness and orientation. In Type-I composites, the decrease in  $\mu$  and wear rate ( $WR$ ) with laminate thickness was more pronounced in the perpendicular orientation as compared to the parallel orientation. Comparatively, Ni- $Ti_3SiC_2$ /Al/Ni composites showed that the parallel orientation was more effective in enhancing the triboactive performance. SEM analysis of tribosurfaces showed signs of tribooxidation and abrasion, which led to the formation of O-rich tribofilms.

**Keywords:** multilayered composites; MAX phases; Ni-matrix composites

## 1. Introduction

There is a critical need for designing lightweight, high-performance materials with high strength and toughness for automotive, aerospace, bioengineering, and construction applications. In general, it is often complicated to design microstructures with the required strength and toughness simultaneously. Nature, however, has long developed the ability to combine brittle minerals and organic molecules into hybrid composites with exceptional fracture resistance and structural capabilities by forming multilayered structures [1]. For example, nacre, bamboo, bone, mantis shrimp club, and elk antler possess exceptional mechanical properties [2]. Fundamental research on layered materials like metal and/or ceramic multilayers has shown great promise due to their unique mechanical, physical, and chemical properties [3,4]. Recently, naturally nanolaminate ceramics like MAX phases have shown promise for designing intricate workpieces subjected to adverse thermal, chemical, and mechanical conditions [5–12].

Thermodynamically stable  $M_{n+1}AX_n$  (MAX) phases possess a  $M_{n+1}AX_n$  chemistry, where  $n = 1, 2, \text{ or } 3$ ; M is an early transition metal element; A is an A-group element (mostly IIIA and IVA);

and X is C and/or N. MAX phases are novel ternary carbides and nitrides that are bestowed with excellent properties like damage tolerance, thermal shock resistance, and machinability [6–12]. Further studies of composites of MAX phases with metals have shown many promising properties [10–22]. For example, Zhang et al. [10] showed that Cu/Ti<sub>3</sub>SiC<sub>2</sub> is self-lubricating and can be a potential electro-friction material [10]. Anasori et al. [11] fabricated Ti<sub>2</sub>AlC–Mg composites by using a melt infiltration method. These composites were easy to process and were lighter than the comparable TiC based composites. Composites of MAX phases with Ag have shown excellent solid lubrication behavior over a wide range of temperatures [12,13]. Wang et al. [14] showed that composites of pure Al reinforced with 40 vol % Ti<sub>3</sub>AlC<sub>2</sub> had twice yield strength than pure aluminum [14]. This group also proved that Ti<sub>3</sub>AlC<sub>2</sub> particulates can efficiently reinforce the Al-matrix. Hu et al. [15] designed Ti<sub>2</sub>AlC/Al composites that had 10 times higher yield strength than peak-aged Al alloy at ambient temperature. These composites were also shown to be stable until 400 °C. Kothalkar et al. [16] also showed that it is viable to design NiTi/Ti<sub>3</sub>SiC<sub>2</sub> composites by sintering at 1233 K, 300 MPa, and 8 min by spark plasma sintering (SPS). Agne et al. [17] showed that composites of Al–V<sub>2</sub>AlC can be synthesized by quenching from 1000 °C. Gupta et al. [18,19] showed that with the addition of Ti<sub>3</sub>SiC<sub>2</sub> particulates in metal matrices, such as Al-, Bi-, and Ag-matrices, the mechanical and tribological of these matrices were improved. These composites were referred to as MAX reinforced metals (MRMs). Fuka et al. [20] and Dey et al. [21] fabricated Ni–MoAlB and Ni–Ti<sub>3</sub>SiC<sub>2</sub> composites, respectively, by hot pressing at 240 MPa at 873 K. These compositions also showed improved tribological behavior. Hu et al. [22] designed TiC<sub>x</sub>-Ni<sub>3</sub>(Al,Ti)/Ni alloy composite by reaction between Ti<sub>3</sub>AlC<sub>2</sub> (20 vol % and 40 vol %) and Ni during in-situ hot-pressing route at 1200 °C under 30 MPa. The composites showed higher hardness, toughness, and flexural strength as compared to the Ni-alloy.

Despite intense research and development in metal–MAX composite systems, there has been limited study on the development of multilayered metal–MAX composites, although some progress has been made in textured MAX-phase based multilayers [23–26]. Murugaiah et al. [23] demonstrated that fine Ti<sub>3</sub>SiC<sub>2</sub> powder can be tape-cast. Hu et al. [24,25] also fabricated textured Nb<sub>4</sub>AlC<sub>3</sub> and Ti<sub>3</sub>SiC<sub>2</sub> by using a 12 T magnetic field during slip casting, followed by cold pressing and spark plasma sintering. Mishra et al. [26] also designed textured Ti<sub>3</sub>SiC<sub>2</sub> by electrophoretic deposition. The objective of this paper is to design and characterize novel multilayered composites by interleaving MAX–Ni composites and Ni by using tape casting.

## 2. Experimental Details

### 2.1. Laminate Design

In this paper, two different types of laminate design were studied: (a) composites layers of Ni and Ti<sub>3</sub>SiC<sub>2</sub> (Ni–Ti<sub>3</sub>SiC<sub>2</sub>) interleaved with Ni (Figure 1a, Type-I composites), and (b) Ni–Ti<sub>3</sub>SiC<sub>2</sub> layers interleaved with Al and Ni (Figure 1b, Type-II composites).

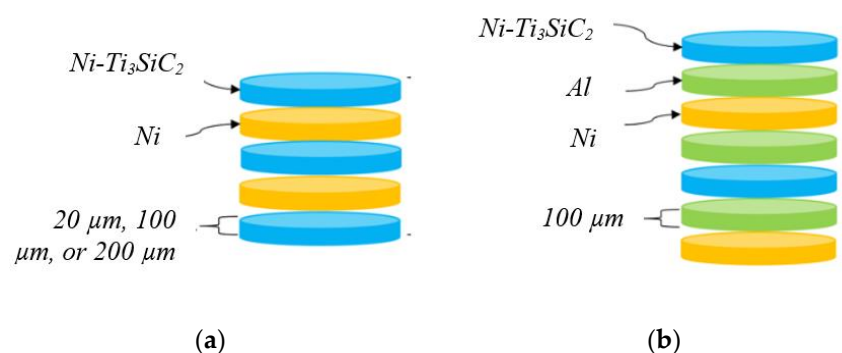


**Figure 1.** Schematics of, (a) Ni–Ti<sub>3</sub>SiC<sub>2</sub>/Ni, and (b) Ni–Ti<sub>3</sub>SiC<sub>2</sub>/Al/Ni multilayered composites.

In Type-I composites, individual layer thickness was varied between 20  $\mu\text{m}$ , 100  $\mu\text{m}$ , or 200  $\mu\text{m}$  when the  $\text{Ti}_3\text{SiC}_2$  content in  $\text{Ni-Ti}_3\text{SiC}_2$  was fixed at 20 vol %. In addition, the  $\text{Ti}_3\text{SiC}_2$  concentration in the  $\text{Ni-Ti}_3\text{SiC}_2$  layers was varied between 10 vol %, 20 vol %, or 40 vol % when the laminate thickness was fixed at 100  $\mu\text{m}$ . These designed compositions are referred to by the following shorthand nomenclature:  $\text{Ni-vol \%Ti}_3\text{SiC}_2/\text{Ni}$  (individual layer thickness).

In Type-II composites, Al layers were inserted between the  $\text{Ni-Ti}_3\text{SiC}_2$  and Ni layers (Figure 1b). In these composites, the concentration of  $\text{Ti}_3\text{SiC}_2$  was kept constant at ~20 vol % in the  $\text{Ni-Ti}_3\text{SiC}_2$  layer, and the thicknesses of the individual laminate layers were either 20  $\mu\text{m}$  or 100  $\mu\text{m}$ , respectively. These designed compositions are referred to by the following shorthand nomenclature:  $\text{Ni-vol \%Ti}_3\text{SiC}_2/\text{Al/Ni}$  (individual layer thickness).

## 2.2. Calculation of $\text{Ti}_3\text{SiC}_2$ Concentration in Composite

The rule of mixture was used to calculate the theoretical density ( $\rho_T$ ) of all the composite samples by using the theoretical density of  $\text{Ti}_3\text{SiC}_2$  and metal components. The experimental density ( $\rho_E$ ) of the composites was then calculated from the mass and dimensions of each sample. Thereafter, the porosity ( $P$  (%)) of the sample was determined by Equation (1):

$$P (\%) = \left(1 - \frac{\rho_E}{\rho_T}\right) \times 100 \quad (1)$$

From calculation perspective, it is important to note the concentrations of  $\text{Ti}_3\text{SiC}_2$  in the  $\text{Ni-Ti}_3\text{SiC}_2$  composites are based on individual layers but not on the vol % of the entire monolithic composites. In other words, the overall volume content of  $\text{Ti}_3\text{SiC}_2$  in multilayered composites is different from that of the isotropic composites with similar chemistry of the individual layers. For example, an isotropic  $\text{Ni-10\%Ti}_3\text{SiC}_2$  with 4 mm thickness will have 10 vol %  $\text{Ti}_3\text{SiC}_2$  dispersed throughout the ~4 mm composite (Figure 2a); however, in multilayered composites, 10%  $\text{Ti}_3\text{SiC}_2$  refers to the concentration of individual layers of  $\text{Ni-Ti}_3\text{SiC}_2$  (Figure 2b).

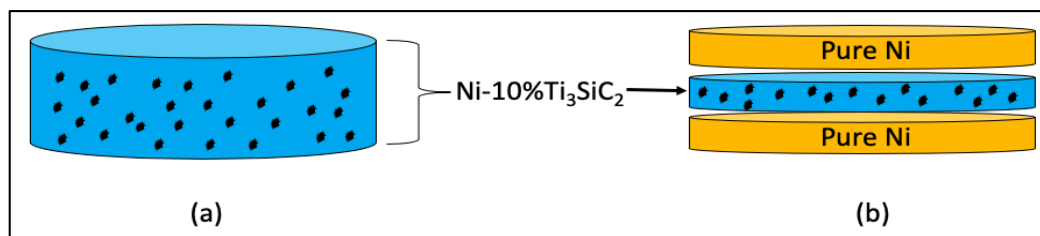


**Figure 2.** Concentration of  $\text{Ti}_3\text{SiC}_2$  in: (a) isotropic  $\text{Ni-Ti}_3\text{SiC}_2$  composites, (b) multilayered  $\text{Ni-Ti}_3\text{SiC}_2$  composites.

Table 1 shows the theoretical calculation of  $\text{Ti}_3\text{SiC}_2$  in the multilayered  $\text{Ni-Ti}_3\text{SiC}_2$  composites with the assumption that the top and bottom layers must be  $\text{Ni-Ti}_3\text{SiC}_2$  layers. The  $\text{Ti}_3\text{SiC}_2$  concentrations mentioned in this paper are 10%, 20%, and 40% of  $\text{Ti}_3\text{SiC}_2$  in the individual layers, not the volume of the composites.

**Table 1.** Concentration of Ni-Ti<sub>3</sub>SiC<sub>2</sub> in multilayered Ni-Ti<sub>3</sub>SiC<sub>2</sub> composites ‡.

Composition	Thickness	Ti <sub>3</sub> SiC <sub>2</sub> Concentration (%)	
		Ni-Ti <sub>3</sub> SiC <sub>2</sub> Layers	Multilayered Ni-Ti <sub>3</sub> SiC <sub>2</sub>
Ni-10%Ti <sub>3</sub> SiC <sub>2</sub> /Ni	100 μm	10%	5.10%
Ni-20%Ti <sub>3</sub> SiC <sub>2</sub> /Ni		20%	10.2%
Ni-40%Ti <sub>3</sub> SiC <sub>2</sub> /Ni		40%	20.5%
Ni-20%Ti <sub>3</sub> SiC <sub>2</sub> /Ni	20 μm	20%	10.05%
Ni-20%Ti <sub>3</sub> SiC <sub>2</sub> /Ni	200 μm	20%	10.5%
Ni-20%Ti <sub>3</sub> SiC <sub>2</sub> /Al/Ni	20 μm	20%	6.80%
Ni-20%Ti <sub>3</sub> SiC <sub>2</sub> /Al/Ni	100 μm	20%	7.00%

‡ This calculation is for qualitative comparison. It is based on the uniform thickness and density of each individual layer.

### 2.3. Slurry Design and Tape Casting

Initially, the binder solution for tape casting was synthesized by dissolving ~20 g poly vinyl alcohol (PVA) (98–99% hydrolyzed, Aldrich Chemistry, St. Louis, MO) in ~80 g distilled water (DI). Dry powders of Ti<sub>3</sub>SiC<sub>2</sub> (–325 mesh, Kanthal, Hallstanhammar, Sweden) and the required concentrations of Ni powder (–325 mesh, Alfa Aesar, Haverhill, MA) were mixed by ball milling (8000 M mixer Mill, SPEX SamplePrep, Metuchen, NJ) for 5 min. The slurry for tape casting was fabricated by mixing dry powders with PVA solution in a 60:40 weight ratio in a ball mill for 5 min. The same protocol was also used for fabricating slurry composed of Ni, Al, and Ti<sub>3</sub>SiC<sub>2</sub> (Type-II composites).

The mixed slurry was then poured onto a mylar polymer film. The poured slurry was then smeared into a single layer by using a tape casting machine (MSK-AFA-111-110, Automatic Thick Film Coater, MTI Corp, Richmond, CA) with a casting speed set at 20 cm/min. The green tapes were then dried at room temperature ~3 h, and then the green film was covered with plywood for ~9 h to prevent warping. The plywood for constraining green tapes was prepared by polishing the plywood with 1200 grit SiC paper and then washing it with acetone. The green tapes were then punched with a circular die of diameter ~25.4 mm. The green tapes were then packed into a dry pressing die (MTI Corp, Richmond, CA) by using the laminate design outlined in Figure 1.

The green body samples were pre-stressed at ~1.49 MPa in a hot press (TF 1200X, MTI Corp, Richmond, CA). The samples were heated at the rate of 10 °C/min to 150 °C, then isothermally held at 150 °C for 5 min. After 5 min, the samples were laminated by hot pressing at a uniaxial pressure of ~119.6 MPa at 150 °C for 5 min. The laminated samples were then allowed to cool to the room temperature; thereafter, the samples were heated to 650 °C at 10 °C/min under a constant pressure of ~1.49 MPa. The samples were isothermally held at 650 °C for 5 min; thereafter, they were hot pressed at ~142 MPa for ~5 min. The composites were then machined into ~3 mm cubes for characterizing mechanical behavior.

### 2.4. Mechanical and Tribological Testing

Compression testing was done by a mechanical testing system (Shimadzu AG-IS UTM, Shimadzu Scientific Instruments Inc., Columbia, MD). For each composition, a set of 6 samples (3 samples each in parallel and perpendicular direction (Figure 3)) were tested at a deflection rate of 1 mm/min. The actual strain of each sample could not be determined due to experimental limitations; hence stress versus displacement plots were reported. For qualitative comparison, ultimate compressive strength (UCS) was defined as the maximum compressive stress after which the sample failed. An average of 3 UCS measurements for each composition at a designed direction was reported in the text.

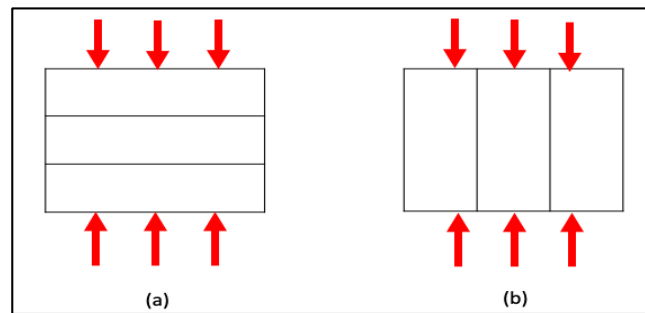


**Figure 3.** Schematics of (a) parallel and (b) perpendicular orientation during mechanical and tribological testing.

For the tribology measurements, all the samples were cut into blocks of  $\sim 4 \text{ mm} \times \sim 4 \text{ mm} \times \sim 3 \text{ mm}$ . Figure 3 shows the orientation of the composite samples at which they were tested; for example, if the layer was aligned parallel or perpendicular to the wear surface then it was referred to as parallel or perpendicular in orientation, respectively. The samples were then polished along those orientations until  $\sim 1 \text{ }\mu\text{m}$  finishing. All the tribology studies were then performed by a block-on-disk tribometer (CSM Instruments SA, Peseux, Switzerland) at a load  $5 \text{ N}$  ( $\sim 0.31 \text{ MPa}$ ), and track radius of  $\sim 10 \text{ mm}$  on alumina substrates at room temperature under ambient conditions, respectively. Alumina substrates (AL-D-42-2, AdValue Technology, Tucson, AZ) were also polished at least  $\sim 3 \text{ }\mu\text{m}$  for finishing. A surface profilometer (Surfcom 480A, Tokyo Seimitsu Co. Ltd., Tokyo, Japan) was used to confirm the surface roughness. For each composition, an average of mean of friction coefficient from three measurements was used to calculate averaged friction coefficient ( $\mu$ ). The mass of the samples and substrates were measured before and after the testing by a weighing scale (XA 83/220/2X, Radwag, Radom, Poland). The specific wear rate ( $WR$ ) was calculated by using Equation (2), where  $m_i$  and  $m_f$  are the mass of the samples before and after testing, respectively,  $N$  is the applied load, and  $d$  is the total distance traversed during the testing [18,19]:

$$WR = (m_i - m_f) / (\rho_T \cdot N \cdot d) \quad (2)$$

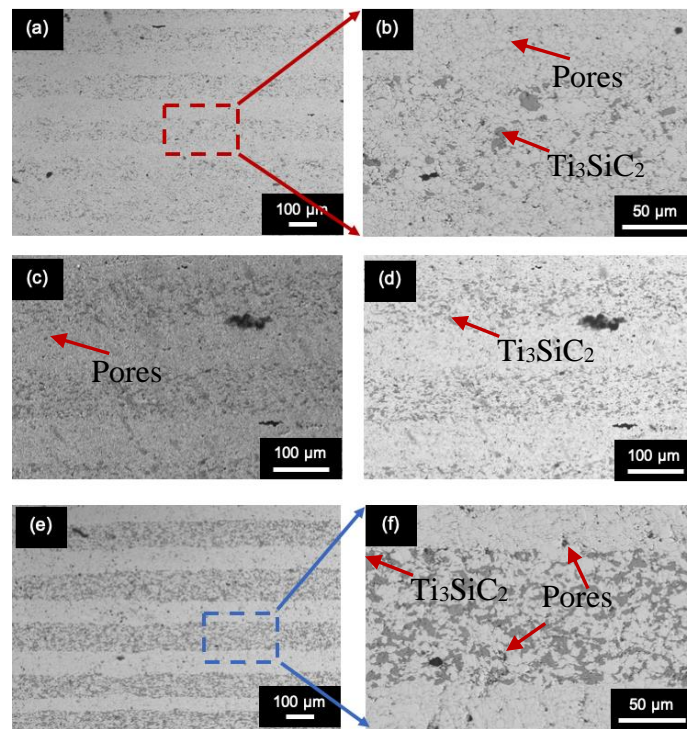
An average of 3  $WR$  readings was reported in the text. For all samples, secondary electron (SE) and backscattered electron (BSE) images were obtained using a JEOL JSM-6490LV scanning electron microscope (JEOL USA, Inc., Peabody, MA, USA). X-ray information was obtained via a thermo nanotracer energy dispersive X-ray detector (EDS) with an NSS-300e acquisition engine. Due to the difficulty in quantifying C by EDS, the C-content of microstructural features was identified by adding  $\{C_x\}$  in the tribochemistry analysis. In addition, the chemically uniform area of tribofilms from BSE images was designated as \*microconstituent\*. The “microconstituent” regions are not necessarily single phase but they are deemed chemically uniform at the micron level by EDS analysis of BSE images [18,19].

### 3. Results and Discussion

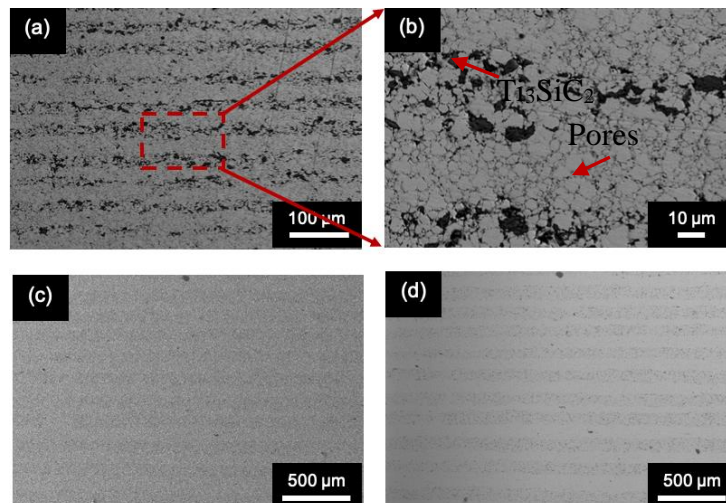
#### 3.1. Microstructure Analysis

Figure 4 shows the microstructures of Ni-10% $\text{Ti}_3\text{SiC}_2/\text{Ni}$  ( $100 \text{ }\mu\text{m}$ ) (Figure 4a,b), Ni-20% $\text{Ti}_3\text{SiC}_2/\text{Ni}$  ( $100 \text{ }\mu\text{m}$ ) (Figure 4c,d), and Ni-40% $\text{Ti}_3\text{SiC}_2/\text{Ni}$  ( $100 \text{ }\mu\text{m}$ ) (Figure 4e,f) composites. In all cases,  $\text{Ti}_3\text{SiC}_2$  particulates were well dispersed in the Ni-layers and the layers were uniform in thickness, although interparticle porosity was observed. In addition, there was no reaction between Ni and  $\text{Ti}_3\text{SiC}_2$  phases. Ni-20% $\text{Ti}_3\text{SiC}_2/\text{Ni}$  ( $20 \text{ }\mu\text{m}$ ) (Figure 5a,b) and Ni-20% $\text{Ti}_3\text{SiC}_2/\text{Ni}$  ( $200 \text{ }\mu\text{m}$ ) (Figure 5c,d) also showed similar microstructures. However, the introduction of Al (Type II) as an interleaving layer between Ni- $\text{Ti}_3\text{SiC}_2$  and Ni in the composite matrix caused interfacial reaction at the interfacial boundary

between Ni and Al (Figure 6). Like Ni-Ti<sub>3</sub>SiC<sub>2</sub>/Ni multilayered composites, Ti<sub>3</sub>SiC<sub>2</sub> particulates were uniformly dispersed in the Ni-matrix and pores were observed in the multilayers.



**Figure 4.** SEM microstructure of (a) Ni-10%Ti<sub>3</sub>SiC<sub>2</sub>/Ni (100 μm) in backscattered electron (BSE) image, (b) BSE image at higher magnifications, (c) Ni-20%Ti<sub>3</sub>SiC<sub>2</sub>/Ni (100 μm) in secondary electron (SE) image, (d) BSE of the same region, (e) Ni-40%Ti<sub>3</sub>SiC<sub>2</sub>/Ni (100 μm) in BSE, and (f) Ni-40%Ti<sub>3</sub>SiC<sub>2</sub>/Ni (100 μm) in BSE at higher magnifications.



**Figure 5.** SEM microstructures of (a) Ni-20%Ti<sub>3</sub>SiC<sub>2</sub>/Ni (20 μm) in BSE, (b) Ni-20%Ti<sub>3</sub>SiC<sub>2</sub>/Ni (20 μm) in BSE at higher magnifications, (c) Ni-20%Ti<sub>3</sub>SiC<sub>2</sub>/Ni (200 μm) in SE, and (d) BSE of the same region.

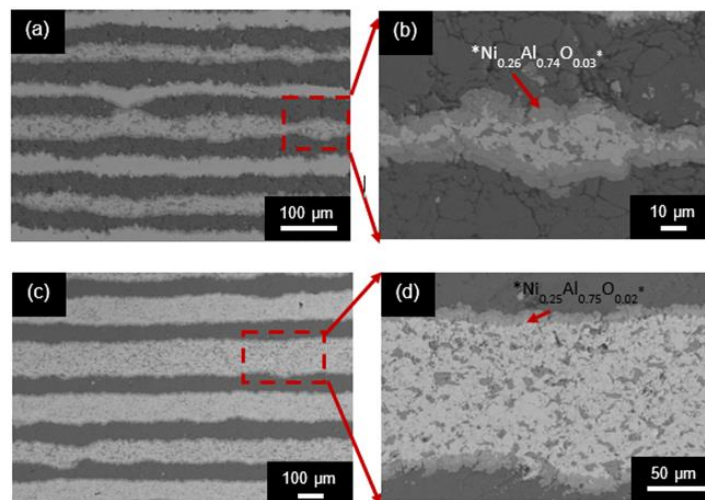


**Figure 6.** SEM microstructure of (a) Ni-20%Ti<sub>3</sub>SiC<sub>2</sub>/Al/Ni (20 μm) in BSE, (b) higher magnification in BSE, (c) Ni-20%Ti<sub>3</sub>SiC<sub>2</sub>/Al/Ni (100 μm) in BSE, and (d) higher magnification in BSE.

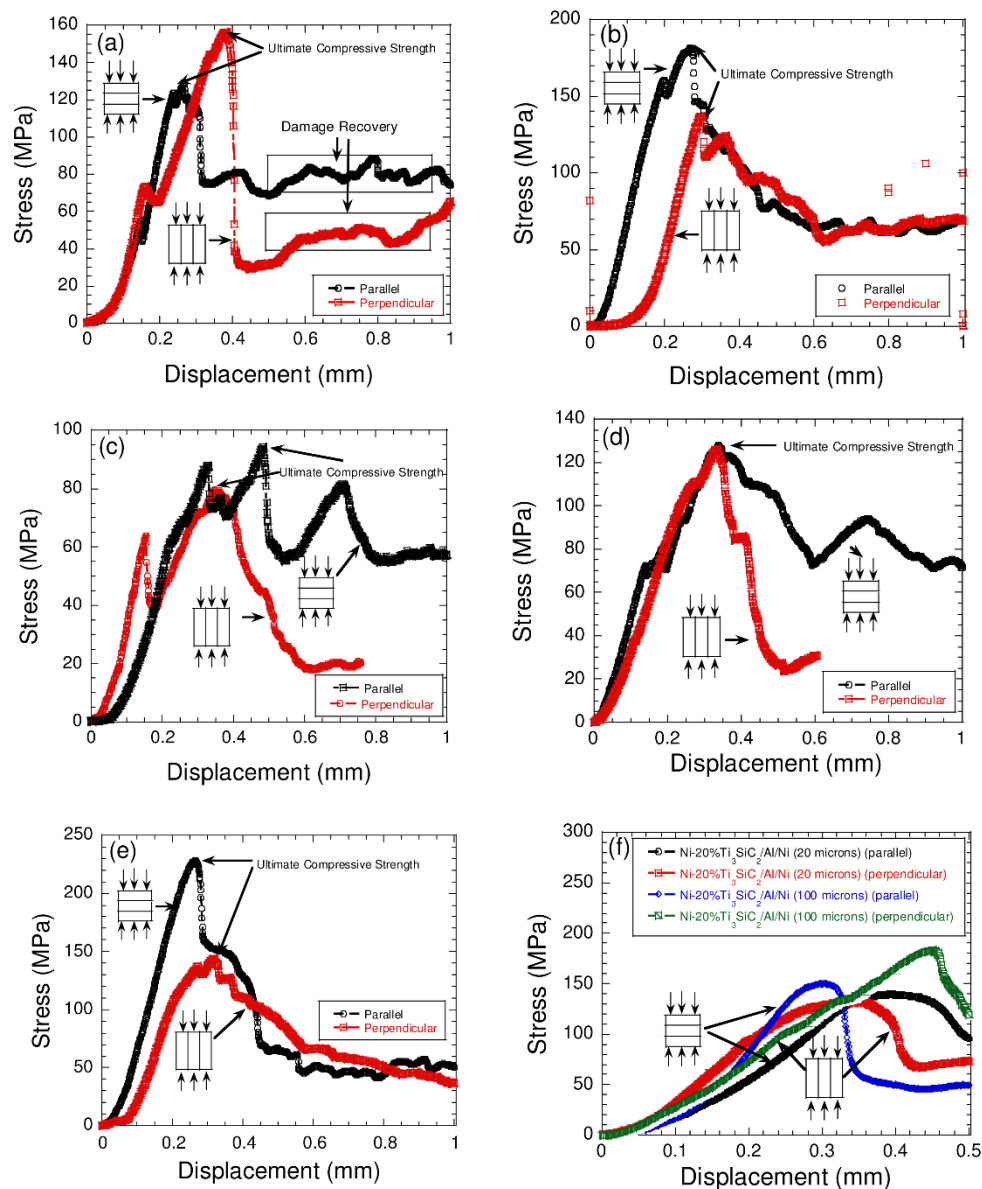
### 3.2. Mechanical Performance of Ni-Matrix Composites

Table 2 summarizes the porosity of multilayered samples. For example, Ni-10%Ti<sub>3</sub>SiC<sub>2</sub>/Ni (100 μm) samples were ~37.6% porous compared to ~32.4% porosity in Ni-40%Ti<sub>3</sub>SiC<sub>2</sub>/Ni (100 μm) compositions. In general, (Ni-20%Ti<sub>3</sub>SiC<sub>2</sub>/Ni) (Al) (Ni) based compositions showed lower porosity due the presence of Al, which helped in densification. The usage of a high binder during tape casting and low processing temperatures can explain the porous nature of these samples.

**Table 2.** Porosity of multilayered samples.

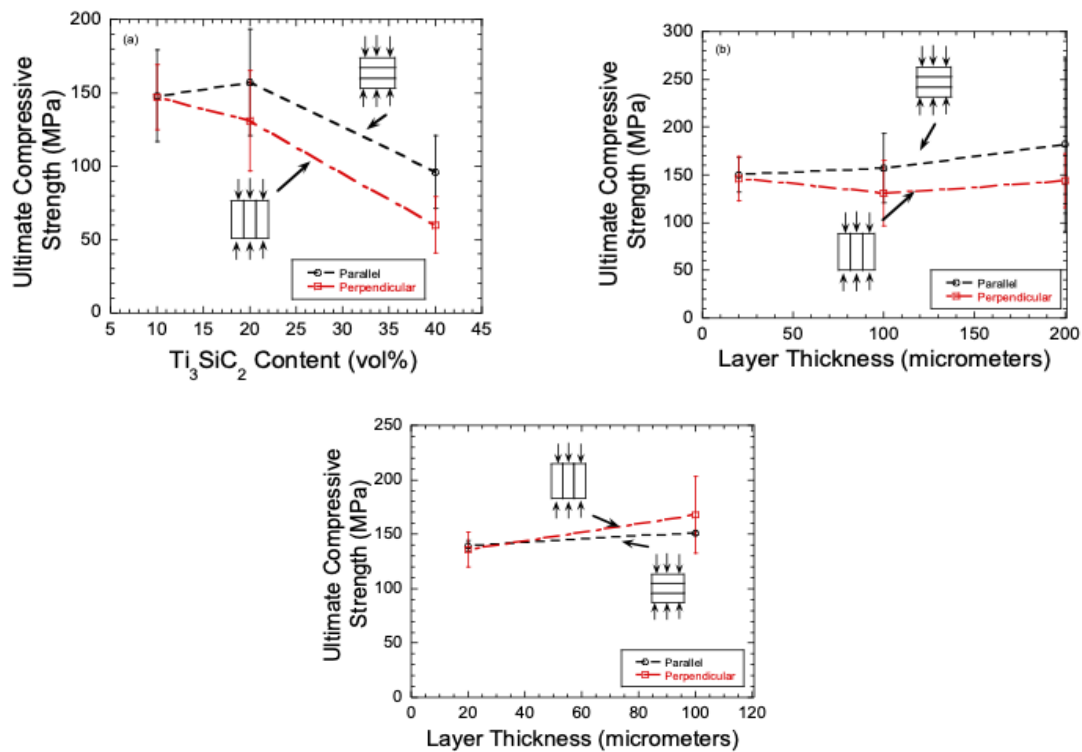
Architecture	Layer Thickness	Porosity
Ni-10%Ti <sub>3</sub> SiC <sub>2</sub> /Ni		37.6 ± 1.28
Ni-20% Ti <sub>3</sub> SiC <sub>2</sub> /Ni	100 μm	27.9 ± 1.34
Ni-40% Ti <sub>3</sub> SiC <sub>2</sub> /Ni		32.4 ± 4.30
Ni-20% Ti <sub>3</sub> SiC <sub>2</sub> /Ni	20 μm	33.4 ± 3.85
Ni-20% Ti <sub>3</sub> SiC <sub>2</sub> /Ni	200 μm	36.8 ± 3.12
(Ni-20% Ti <sub>3</sub> SiC <sub>2</sub> /Ni) (Al) (Ni)	20 μm	29.1 ± 1.00
(Ni-20% Ti <sub>3</sub> SiC <sub>2</sub> /Ni) (Al) (Ni)	100 μm	28.1 ± 1.42

Figure 7 shows the representative plots of stress versus displacement experiments for all the composites. The Ni-Ti<sub>3</sub>SiC<sub>2</sub>/Ni composites showed, in both directions, ductile and gradual failure with some signs of damage recovery. In general, the failure was gradual, although in some cases samples failed rapidly in the perpendicular direction as compared to the parallel direction (Figure 7c,d). This may be attributed to the presence of lamellar defects and/or porosity during the manufacturing process. In the type II composites (Figure 7f), the addition of Al into the composite matrix caused the composites to become ductile, and the failure was gradual in both orientations.



**Figure 7.** Plot of compressive stress versus displacement of (a) Ni-10%Ti<sub>3</sub>SiC<sub>2</sub>/Ni (thickness of laminate is 100 μm), (b) Ni-20%Ti<sub>3</sub>SiC<sub>2</sub>/Ni (thickness of laminate is 100 μm), (c) Ni-40%Ti<sub>3</sub>SiC<sub>2</sub>/Ni (thickness of laminate is 100 μm), (d) Ni-20%Ti<sub>3</sub>SiC<sub>2</sub>/Ni (thickness of laminate is 20 μm), (e) Ni-20%Ti<sub>3</sub>SiC<sub>2</sub>/Ni (thickness of laminate is 200 μm), and (f) Ni-10%Ti<sub>3</sub>SiC<sub>2</sub>/Al/Ni composites with different thicknesses.

Figure 8 shows the ultimate compressive strength (UCS) of all the tested composites. In Type-I composites (Figure 8a), the UCS marginally increased in Ni-20%Ti<sub>3</sub>SiC<sub>2</sub>/Ni (100 μm) to ~157 MPa as compared to ~148 MPa in Ni-10%Ti<sub>3</sub>SiC<sub>2</sub>/Ni (100 μm) in parallel orientation; thereafter, the UCS decreased in Ni-40%Ti<sub>3</sub>SiC<sub>2</sub>/Ni (100 μm) to ~96 MPa, whereas in the perpendicular orientation, the UCS decreased gradually from ~147 MPa in Ni-10%Ti<sub>3</sub>SiC<sub>2</sub>/Ni (100 μm) to ~60 MPa in Ni-40%Ti<sub>3</sub>SiC<sub>2</sub>/Ni (100 μm). The UCS of these composites was sensitive to Ti<sub>3</sub>SiC<sub>2</sub> content, and it decreased as the concentration of Ti<sub>3</sub>SiC<sub>2</sub> was increased in the composites. Comparatively, the decrease in strength with the increase in Ti<sub>3</sub>SiC<sub>2</sub> content was more prominent in perpendicular orientation as compared to the parallel direction, which may be due to the weak interlaminar bonding and/or defects between the multilayers.



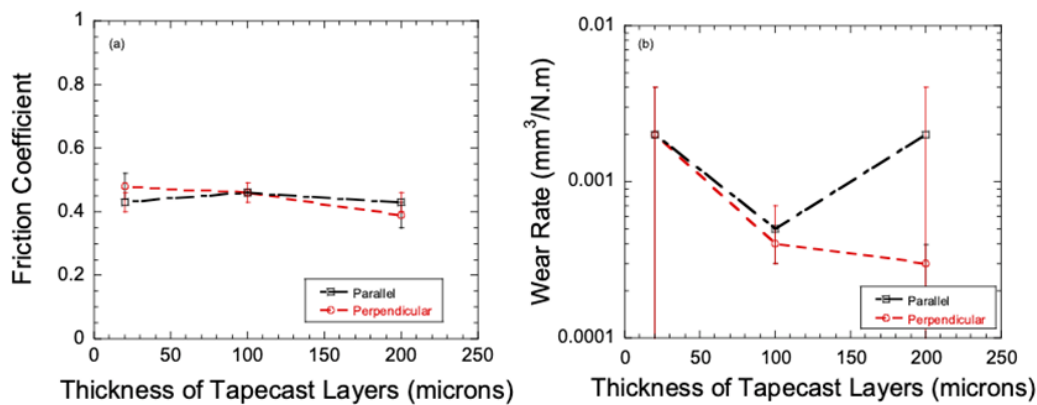
**Figure 8.** Plot of ultimate compressive strength (UCS) versus  $\text{Ti}_3\text{SiC}_2$  content in (a) Ni– $\text{Ti}_3\text{SiC}_2$  (100  $\mu\text{m}$ ), (b) Ni–20% $\text{Ti}_3\text{SiC}_2$ /Ni, and (c) Ni– $\text{Ti}_3\text{SiC}_2$ /Al/Ni multilayered composites.

In another study, the concentration of  $\text{Ti}_3\text{SiC}_2$  in Type-I composites was fixed at 20 vol %, and the layer thickness was varied from 20  $\mu\text{m}$  to 200  $\mu\text{m}$  in Ni– $\text{Ti}_3\text{SiC}_2$ /Ni composites. The UCS increased from ~150 MPa to ~182 MPa in the parallel direction, whereas in the perpendicular direction, the UCS was slightly lower but the samples had similar strength, for example ~146 MPa and ~144 MPa in Ni–20% $\text{Ti}_3\text{SiC}_2$ /Ni (20  $\mu\text{m}$ ) and Ni–20% $\text{Ti}_3\text{SiC}_2$ /Ni (200  $\mu\text{m}$ ), respectively (Figure 8b). This study shows that the UCS increased in the parallel orientation but retained lower and similar strength values in the perpendicular orientation as the laminate thickness was increased from 20  $\mu\text{m}$  to 200  $\mu\text{m}$ , which further supports the hypothesis that the laminates are weakly bonded and/or defects are present between the multilayers.

In Type-II composites (Figure 8c), where the concentration of  $\text{Ti}_3\text{SiC}_2$  was fixed at 20 vol % in the laminates (Table 1), the UCS increased from ~139 MPa to ~151 MPa, and from ~136 MPa to ~168 MPa in parallel and perpendicular orientations, respectively, as the layer thickness was increased from 20  $\mu\text{m}$  to 100  $\mu\text{m}$ . Unlike Type-I composites, this study shows that the UCS was greater in perpendicular orientation as compared to parallel due to the presence of Al as bonding layers. In addition, UCS also increased for both orientations as the laminate thickness was increased from 20  $\mu\text{m}$  to 100  $\mu\text{m}$ . Like Type I composites, this observation also supports the hypothesis that the laminates are weakly bonded and/or defects are present between the multilayers as UCS was lower in samples with finer laminate thickness.

### 3.3. Tribological Behavior of Ni– $\text{Ti}_3\text{SiC}_2$ Composites

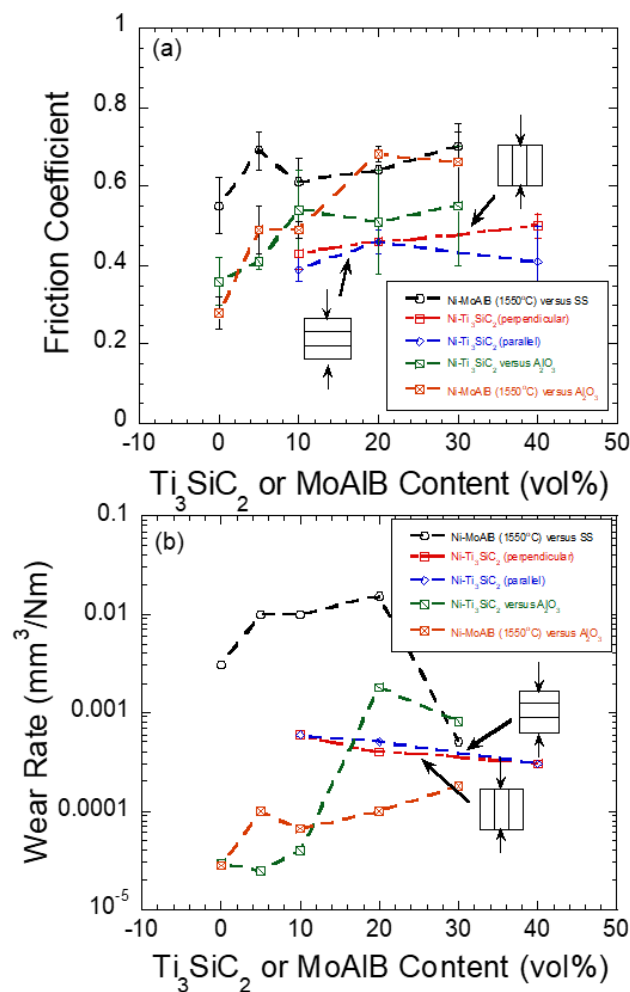
Figure 9 shows the plot of  $\mu$  and WR in Ni–20% $\text{Ti}_3\text{SiC}_2$ /Ni (Type I) composites. As the laminate thickness was increased from 20 to 100  $\mu\text{m}$ , the  $\mu$  slightly increased in the parallel direction from ~0.43 to ~0.46; thereafter, it decreased to ~0.43 when the layer thickness was further increased to 200  $\mu\text{m}$ . However, in the perpendicular direction, the same composites showed a steady decline in  $\mu$  from ~0.46 to ~0.39 when the layer thickness was varied from ~20  $\mu\text{m}$  to ~200  $\mu\text{m}$ , respectively.



**Figure 9.** Plot of (a) friction coefficient, and (b) wear rate (*WR*) of Ni-20%Ti<sub>3</sub>SiC<sub>2</sub>/Ni multilayered composites as a function of laminate thickness.

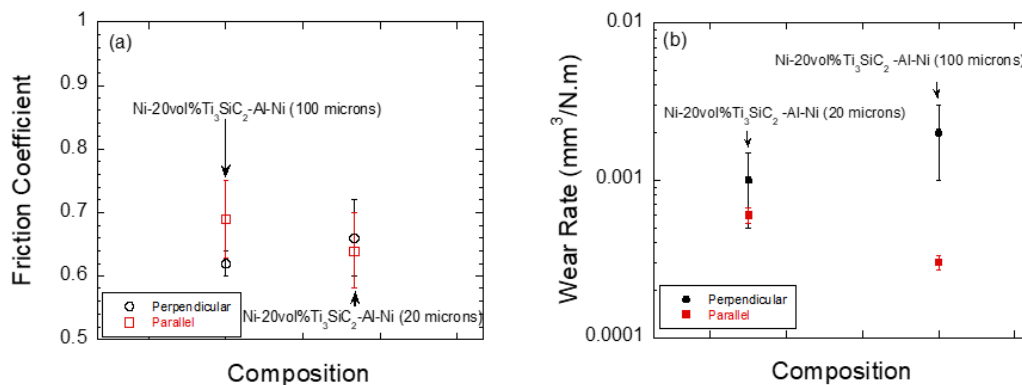
In the parallel orientation, the *WR* decreased from  $\sim 2 \times 10^{-3} \text{ mm}^3/\text{Nm}$  in Ni-20%Ti<sub>3</sub>SiC<sub>2</sub>/Ni (20  $\mu\text{m}$ ) to  $\sim 5 \times 10^{-4} \text{ mm}^3/\text{Nm}$  in Ni-20%Ti<sub>3</sub>SiC<sub>2</sub>/Ni (100  $\mu\text{m}$ ), but then sharply increased to  $\sim 2 \times 10^{-3} \text{ mm}^3/\text{Nm}$  in Ni-20%Ti<sub>3</sub>SiC<sub>2</sub>/Ni (200  $\mu\text{m}$ ). The *WR* decreased by one order of magnitude from  $\sim 2 \times 10^{-3} \text{ mm}^3/\text{Nm}$  in Ni-20%Ti<sub>3</sub>SiC<sub>2</sub>/Ni (20  $\mu\text{m}$ ) to  $\sim 4 \times 10^{-4} \text{ mm}^3/\text{Nm}$  in Ni-20%Ti<sub>3</sub>SiC<sub>2</sub>/Ni (100  $\mu\text{m}$ ) and  $\sim 3 \times 10^{-4} \text{ mm}^3/\text{Nm}$  in Ni-20%Ti<sub>3</sub>SiC<sub>2</sub>/Ni (200  $\mu\text{m}$ ), respectively, in the perpendicular orientation. By analyzing the  $\mu$  and *WR*, the following points can be summarized: (a) the decrease in  $\mu$  and *WR* was more pronounced in the perpendicular orientation, as it was easier to supply solid lubricants from individual layers as compared to parallel orientations where the interleaving layers were Ni; and (b) tribological behavior showed sensitivity to laminate thickness; for example, Ni-20%Ti<sub>3</sub>SiC<sub>2</sub>/Ni (100  $\mu\text{m}$ ) showed optimum *WR* in both orientations.

Figure 10 summarizes the  $\mu$  and *WR* of Ni-Ti<sub>3</sub>SiC<sub>2</sub>/Ni (100  $\mu\text{m}$ ) composites against alumina disks as compared to the monolithic Ni-Ti<sub>3</sub>SiC<sub>2</sub>, and Ni-MoAlB disks against stainless steel and alumina balls [20,21] (please note, tribological results are dependent on testing parameters; hence the results are for qualitative comparison). During both orientations, the multilayered composites had lower  $\mu$  than the monolithic Ni-Ti<sub>3</sub>SiC<sub>2</sub> and Ni-MoAlB. To summarize, in the perpendicular orientation, the  $\mu$  increased from  $\sim 0.43$  to  $\sim 0.50$  as the Ti<sub>3</sub>SiC<sub>2</sub> content was increased from 10 to 40 vol % (Figure 10a), and the *WR* decreased marginally from  $\sim 0.0006 \text{ mm}^3/\text{Nm}$  to  $\sim 0.0003 \text{ mm}^3/\text{Nm}$  (Figure 10b). In the parallel orientation, the  $\mu$  increased from  $\sim 0.39$  to  $\sim 0.41$ , and the *WR* decreased from  $\sim 0.0006 \text{ mm}^3/\text{Nm}$  to  $\sim 0.0003 \text{ mm}^3/\text{Nm}$  as the Ti<sub>3</sub>SiC<sub>2</sub> content was increased from 10 to 40 vol %, respectively. In both orientations, Ti<sub>3</sub>SiC<sub>2</sub> content was effective in decreasing the *WR* marginally, but  $\mu$  was marginally increased. Follow up studies are needed to understand the effect of texture and porosity on the tribological behavior of these composites.



**Figure 10.** Plot of (a) friction coefficient, and (b) wear rate as a function of  $Ti_3SiC_2$  content in Ni- $Ti_3SiC_2$ /Ni composites (laminar thickness in all composites was 100  $\mu m$ ) [20,21].

Figure 11 shows the plot of  $\mu$  and  $WR$  of Ni- $Ti_3SiC_2$ /Al/Ni multilayered composites. The plot shows that there was an increase in  $\mu$  due to the addition of interleaving Al-layers as compared to Type-I composites. The  $WR$  also increased from  $\sim 0.001 mm^3/Nm$  to  $\sim 0.002 mm^3/Nm$  in the perpendicular direction as the layer thickness was increased from 20  $\mu m$  to 100  $\mu m$ , respectively. However, in the parallel orientation, the  $WR$  decreased from  $\sim 0.0006 mm^3/Nm$  to  $\sim 0.0003 mm^3/Nm$  as the layer thickness was increased from 20  $\mu m$  to 100  $\mu m$ , respectively. This behavior was different from Type-I (Ni- $Ti_3SiC_2$ /Ni) composites where the perpendicular orientation was more effective in enhancing the triboactive performance as the laminar thickness was changed systematically.



**Figure 11.** Comparative plot of (a) friction coefficient, and (b) WR of Ni-Ti<sub>3</sub>SiC<sub>2</sub>/Al/Ni multilayered composites.

The possible reason is that the Al-layers were more effective in shearing during parallel orientation as compared to the perpendicular orientation, which could cause a lower WR. In addition, the overall concentration of Ti<sub>3</sub>SiC<sub>2</sub> in the Ni-20%Ti<sub>3</sub>SiC<sub>2</sub>/Al/Ni (20 or 100 μm) was lower than the effective Ti<sub>3</sub>SiC<sub>2</sub> concentration in Ni-20%Ti<sub>3</sub>SiC<sub>2</sub>/Ni composites; thus, less amount of solid lubricant was available during sliding in the perpendicular orientation (Table 1).

Figure 12a–d show the Ni-20%Ti<sub>3</sub>SiC<sub>2</sub>/Ni (100 μm) composite and alumina surfaces after tribological testing in the parallel orientation. On both surfaces, there were signs of abrasive and oxidative wear. For example, the tribosurface of Ni-20%Ti<sub>3</sub>SiC<sub>2</sub>/Ni (100 μm) was partially oxidized (\*NiO<sub>0.03</sub>{C<sub>x</sub>}\*), Figure 12b) and powdered wear debris (\*Ni<sub>0.96</sub>Ti<sub>0.03</sub>Si<sub>0.01</sub>O<sub>0.027</sub>{C<sub>x</sub>}\*), Figure 12d) was observed on the alumina surface, respectively. Similarly, Figure 13a–d show the Ni-20%Ti<sub>3</sub>SiC<sub>2</sub>/Ni (100 μm) composite in the perpendicular direction. Similar oxidative tribochemical reactions and powdered/smearred wear debris were observed on these surfaces too. Figures 14 and 15 show Ni-20%Ti<sub>3</sub>SiC<sub>2</sub>/Al/Ni (100 μm) (Type II) composite in both parallel and perpendicular orientations after testing, respectively. All the surfaces showed signs of heavy abrasive and oxidative wear. Clearly, the formation of oxidized tribofilms played an important role in the tribological behavior of these composites. More studies are needed to understand the correlation between tribofilm formation and tribological behavior in these composites.

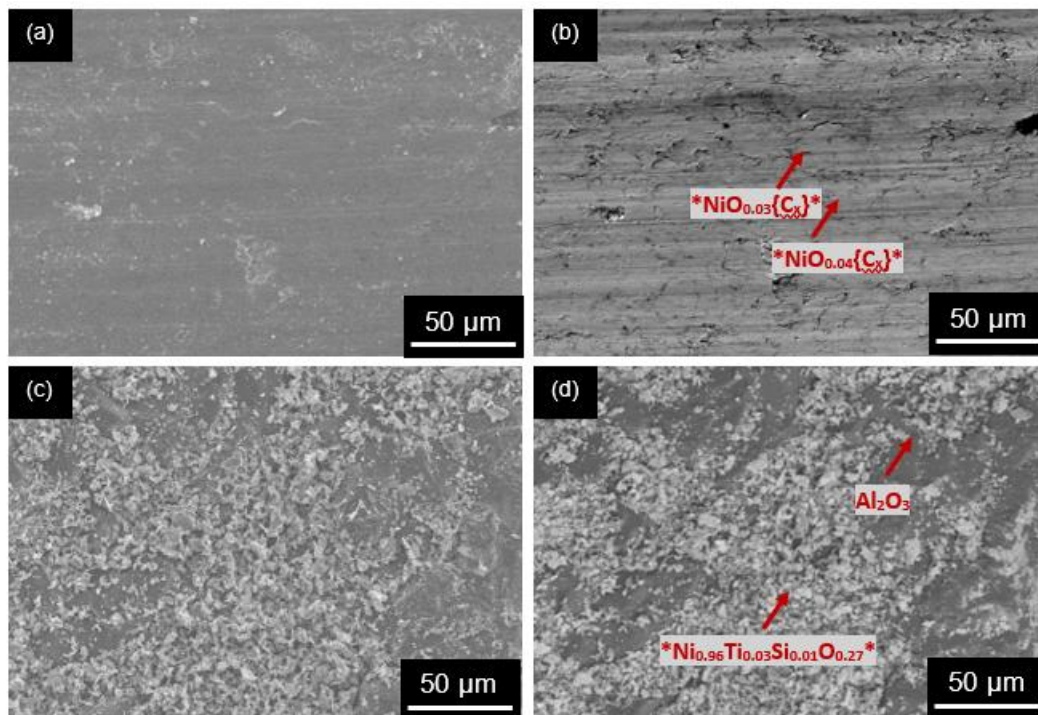


**Figure 12.** SEM micrographs of (a) Ni-20%Ti<sub>3</sub>SiC<sub>2</sub>/Ni (100 μm) surface in SE, (b) BSE of the same region, (c) alumina surface in SE, and (d) BSE of the same region after tribological testing in parallel orientation.

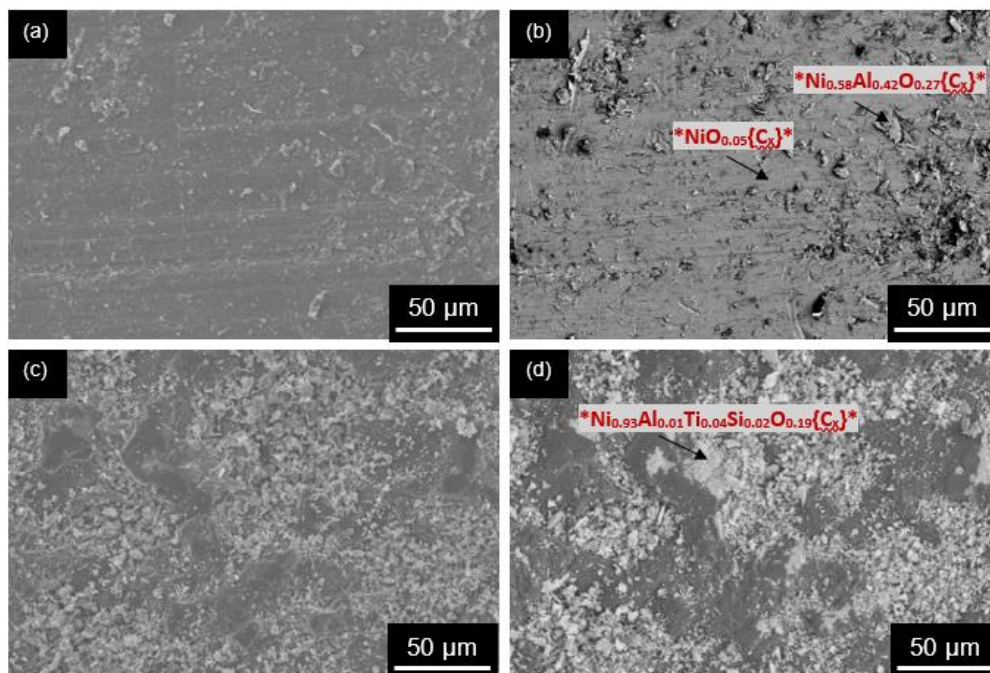


**Figure 13.** SEM micrographs of (a) Ni-20%Ti<sub>3</sub>SiC<sub>2</sub>/Ni (100 μm) surface (perpendicular to the casting direction) in SE, (b) BSE of the same region, (c) alumina surface in SE, and (d) BSE of the same region after tribological testing in perpendicular orientation.

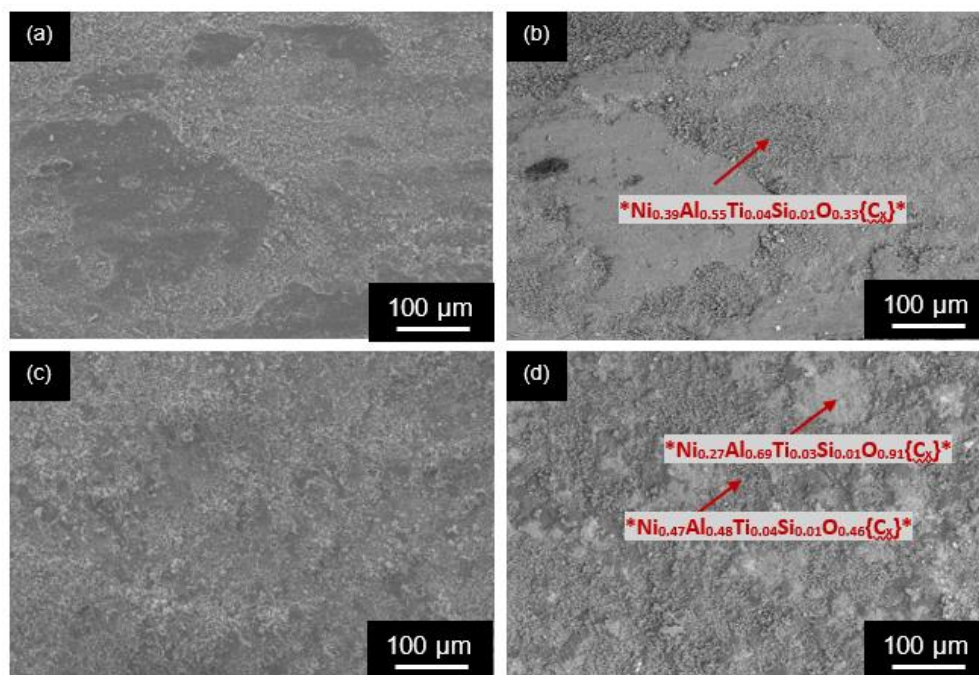


**Figure 14.** SEM micrographs of (a) Ni-20%Ti<sub>3</sub>SiC<sub>2</sub>/Al/Ni (100 μm) surface (parallel orientation) in SE, (b) BSE of the same region, (c) alumina surface in SE, and (d) BSE of the same region after tribological testing.

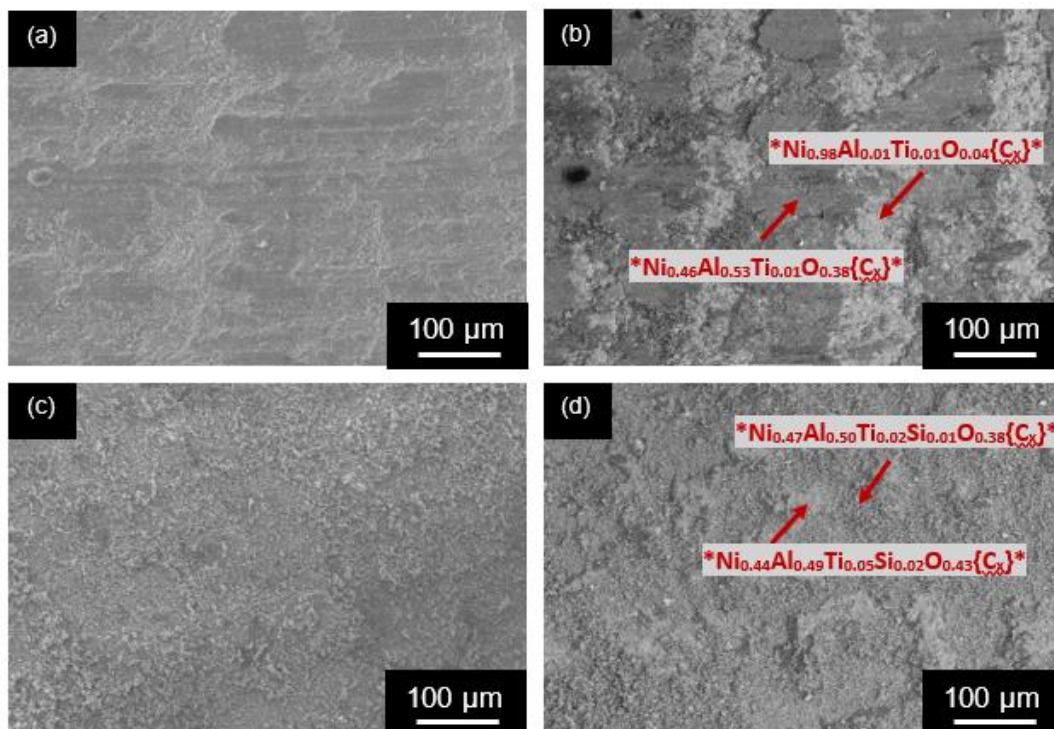


**Figure 15.** SEM micrographs of (a) Ni-20%Ti<sub>3</sub>SiC<sub>2</sub>/Al/Ni (100 μm) surface (perpendicular to the casting direction) in SE, (b) BSE of the same region, (c) alumina surface in SE, and (d) BSE of the same region after tribological testing.

### 3.4. Comparison with Other Solid Lubricants

Single component solid lubricants like MnS and graphite are very promising for different wear resistant applications [27,28]. However, they cannot be used in high temperature applications due to

issues like oxidation, matrix evaporation, etc. For high performance applications, Ni-based binary compositions have been studied; for example, the *WR* of NiCr–Al<sub>2</sub>O<sub>3</sub> composites varied in the range of  $(1\text{--}2) \times 10^{-4}$  mm<sup>3</sup>/Nm at RT as the Al<sub>2</sub>O<sub>3</sub> content in NiCr was varied from 20 to 60 wt %, but the friction coefficient was relatively high (0.7–0.8) in all the compositions during testing by ball-on-disk method [29]. In order to further enhance the tribological behavior of Ni-based compositions, multicomponent Ni-based solid lubricants have been studied. For example, Dellacorte et al. [30,31] developed PS-300 (NiCr–Cr<sub>2</sub>O<sub>3</sub> (80.3 vol %), Ag (5.5 vol %), CaF<sub>2</sub>/BaF<sub>2</sub> (14.2 vol %)) and PS-400 ((NiMoAl (70 wt %)–Cr<sub>2</sub>O<sub>3</sub> (20 wt %)–Ag (5 wt %)–BaF<sub>2</sub>/CaF<sub>2</sub> (5 wt %))) coating. These materials have shown promise, and the *WR* was in the range of  $10^{-3}$ – $10^{-4}$  mm<sup>3</sup>/Nm during testing at room temperature [30,31]. Similarly, other multicomponent solid lubricant systems like ZrO<sub>2</sub> (Y<sub>2</sub>O<sub>3</sub>)–Mo–BaF<sub>2</sub>/CaF<sub>2</sub> composites have also been studied with *WR* in the range of  $10^{-4}$  mm<sup>3</sup>/Nm [32]. From the perspective of reproducibility, large scale commercialization, and rapid deployment, it is vital to design simpler compositions that can be manufactured easily. By fabricating composites from multilayers, it is possible to tailor the microstructure while keeping the composition simpler. The present research shows that the multilayered Ni-based composites offer us a new design paradigm for fabricating effective solid lubricants by using only binary constituents.

#### 4. Conclusions

In this paper, two different types of laminate design were successfully synthesized: (a) Composite layers of Ni and Ti<sub>3</sub>SiC<sub>2</sub> (Ni–Ti<sub>3</sub>SiC<sub>2</sub>) were interleaved with Ni (Figure 1a, Type-I composites), and (b) Ni–Ti<sub>3</sub>SiC<sub>2</sub> layers were interleaved with Al and Ni (Figure 1b, Type-II composites). Detailed SEM studies showed that Ti<sub>3</sub>SiC<sub>2</sub> particulates were well distributed in the Ni-matrix with little or no interfacial reactions along with the presence of interparticle porosity. However, there were interfacial reactions between Ni and Al in Type II composites.

Type I (Ni–Ti<sub>3</sub>SiC<sub>2</sub>/Ni) multilayered composites had higher UCS in parallel orientation as compared to perpendicular orientation. Most likely the presence of interlaminar defects and/or weak interlaminar bonding can account for this observation. Comparatively, in Type II (Ni–Ti<sub>3</sub>SiC<sub>2</sub>/Al/Ni) composites, the UCS was greater in the perpendicular orientation as compared to the parallel due to the presence of interleaving Al as bonding layers, which are effective in increasing the UCS of these materials.

In Type I (Ni–Ti<sub>3</sub>SiC<sub>2</sub>/Ni) composites, (a) the decrease in  $\mu$  and *WR* was more pronounced in perpendicular orientation as it much easier to supply solid lubricants from individual layers compared to parallel orientations where the interleaving layers are Ni, and (b) tribological behavior showed sensitivity to laminate thickness; for example, Ni-20%Ti<sub>3</sub>SiC<sub>2</sub>/Ni (100  $\mu$ m) showed optimum *WR* in both orientations. Comparatively, Type II (Ni–Ti<sub>3</sub>SiC<sub>2</sub>/Al/Ni) composites showed that the parallel orientation was more effective in enhancing the triboactive performance. Most probably, Al-layers are more effective in shearing during parallel orientation as compared to the perpendicular orientation, which can cause a lower *WR* in these composites. In addition, the overall concentration of Ti<sub>3</sub>SiC<sub>2</sub> in Type-II is lower than the effective Ti<sub>3</sub>SiC<sub>2</sub> concentration in Type-I composites; thus, a lesser amount of solid lubricant is available during the perpendicular orientation.

**Author Contributions:** Conceptualization, Q.T. and S.G.; methodology, Q.T. and S.G.; validation, Q.T., M.F., M.D. and S.G.; formal analysis, Q.T., M.F., M.D. and S.G.; investigation, Q.T., M.F., M.D. and S.G.; resources, Q.T., M.F., M.D. and S.G.; data curation, Q.T., M.F., M.D. and S.G.; writing—original draft preparation, Q.T., M.F., M.D. and S.G.; writing—review and editing, Q.T., M.F., M.D. and S.G.; supervision, S.G.; project administration, S.G.; funding acquisition, S.G.

**Funding:** CRADA with Army Research Labs (ARL) and University of North Dakota is acknowledged for support.

**Acknowledgments:** Caleb Matzke is acknowledged for performing mechanical testing.

**Conflicts of Interest:** The authors declare no conflict of interest.

## References

- Munch, E.; Launey, M.E.; Alsem, D.H.; Saiz, E.; Tomsia, A.P.; Ritchie, R.O. Tough, bio-Inspired Hybrid Materials. *Science* **2008**, *322*, 1516–1520. [[CrossRef](#)] [[PubMed](#)]
- Askarinejad, S.; Rahbar, N. Mechanics of Bioinspired Lamellar structured ceramic/polymer Composites: Experiments and Models. *Int. J. Plast.* **2018**, *107*, 122–149. [[CrossRef](#)]
- Salehinia, I.; Shao, S.; Wang, J.; Zbib, H.M. Plastic Deformation of Metal/Ceramic Nanolayered Composites. *JOM* **2014**, *66*, 2078–2085. [[CrossRef](#)]
- Clegg, W.J.; Kendall, K.; Alford, N.M.; Button, T.W.; Birchall, J.D. A simple way to make tough ceramics. *Nature* **1990**, *347*, 455–457. [[CrossRef](#)]
- Prikhna, T.A.; Dub, S.N.; Starostina, A.V.; Karpets, M.V.; Cabiosh, T.; Chartier, P. Mechanical Properties of Material Based on MAX Phases of the Ti-Al-C System. *J. Superhard Mater.* **2012**, *34*, 102–109. [[CrossRef](#)]
- Barsoum, M.W.; Radovic, M. Elastic and Mechanical Properties of the MAX Phases. *Annu. Rev. Mater. Res.* **2011**, *41*, 195–197. [[CrossRef](#)]
- Barsoum, M.W. The  $M_{n+1}AX_n$  Phases: A New Class of Solids; Thermodynamically Stable Nanolaminates. *Prog. Solid State Chem.* **2000**, *28*, 201–281. [[CrossRef](#)]
- Barsoum, M.W.; El-Raghy, T. Synthesis and Characterization of Remarkable Ceramic,  $Ti_3SiC_2$ . *J. Am. Ceram. Soc.* **1996**, *79*, 1953–1956. [[CrossRef](#)]
- Amini, S.; Barsoum, M.W.; El-Raghy, T. Synthesis and Mechanical Properties of Fully Dense  $Ti_2SC$ . *J. Am. Ceram. Soc.* **2007**, *90*, 3953–3958. [[CrossRef](#)]
- Zhang, Y.; Sun, Z.M.; Zhou, Y.C.  $Cu/Ti_3SiC_2$  Composites: A New Electrofriction Material. *Mater. Res. Innov.* **1999**, *3*, 80–84. [[CrossRef](#)]
- Anasori, B.; El'ad, N.C.; Barsoum, M.W. Fabrication and mechanical properties of pressureless melt infiltrated magnesium alloy composites reinforced with TiC and  $Ti_2AlC$  particles. *Mater. Sci. Eng. A* **2014**, *618*, 511–522. [[CrossRef](#)]
- Gupta, S.; Barsoum, M.W. On the Tribology of the MAX Phases and Their Composites During Dry Sliding: A Review. *Wear* **2011**, *271*, 1878–1894. [[CrossRef](#)]
- Gupta, S.; Filimonov, D.; Palanisamy, T.; El-Raghy, T.; Barsoum, M.W.  $Ta_2AlC$  and  $Cr_2AlC$  Ag-based Composites: New Solid Lubricant Materials for use Over a Wide Temperature Range Against Ni-Based Superalloys and Alumina. *Wear* **2007**, *262*, 1479–1489. [[CrossRef](#)]
- Wang, W.J.; Gauthier-Brunet, V.; Bei, G.P.; Laplanche, G.; Bonneville, J.; Joulain, A.; Dubois, S. Powder Metallurgy Processing and Compressive Properties of  $Ti_3AlC_2/Al$  Composites. *Mater. Sci. Eng. A* **2011**, *530*, 168–173. [[CrossRef](#)]
- Hu, L.; O'Neil, M.; Erturun, V.; Benitez, R.; Proust, G.; Karaman, I.; Radovic, M. High-Performance Metal/Carbide Composites with Far-From Equilibrium Compositions and Controlled Microstructures. *Sci. Rep.* **2016**, *6*, 35523. [[CrossRef](#)]
- Kothalkar, A.; Karaman, I.; Radovic, M. Fabrication and characterization of  $NiTi/Ti_3SiC_2$  and  $NiTi/Ti_2AlC$  composites. *J. Alloys Compd.* **2014**, *610*, 635–644.
- Agne, M.T.; Radovic, M.; Bentzel, G.W.; Barsoum, M.W. Stability of  $V_2AlC$  with Al in 800–1000 °C temperature range and in situ synthesis of  $V_2AlC/Al$  composites. *J. Alloys Compd.* **2016**, *666*, 279–286. [[CrossRef](#)]
- Gupta, S.; Hammann, T.; Johnson, R.; Riyad, M.F. Synthesis and Characterization of Novel Al-Matrix Composites Reinforced with  $Ti_3SiC_2$  Particulates. *J. Mater. Eng. Perform.* **2014**, *24*, 1011–1017. [[CrossRef](#)]
- Gupta, S.; AlAnazi, F.; Ghosh, S.; Dunnigan, R. Synthesis and Tribological Behavior of Novel Ag- and Bi-Based Composites Reinforced with  $Ti_3SiC_2$ . *Wear* **2017**, *376*, 1074–1083.
- Fuka, M.; Dey, M.; Gupta, S. Novel Ternary Boride ( $MoAlB$ ) Particulates as Solid Lubricant Additives in Ni-matrix Composites. In Proceedings of the 2018 Joint Propulsion Conference, Session: Additive Manufacturing for Propulsion Systems II, AIAA 2018-4893, Cincinnati, OH, USA, 9–11 July 2018. [[CrossRef](#)]
- Dey, M.; Fuka, M.; AlAnazi, F.; Gupta, S. Synthesis and Characterization of Novel  $Ni-Ti_3SiC_2$  Composites. In Proceedings of the 42nd International Conference on Advanced Ceramics and Composites, Daytona Beach, FL, USA, 21–26 January 2018; pp. 105–116.
- Hu, W.; Huang, Z.; Cai, L.; Lei, C.; Zhai, H.; Hao, S.; Yu, W.; Zhou, Y. “Preparation and mechanical properties of  $TiC_x-Ni_3(Al,Ti)/Ni$  composites synthesized from Ni alloy and  $Ti_3AlC_2$  powders”. *Mater. Sci. Eng. A* **2017**, *697*, 48–54. [[CrossRef](#)]

23. Murugaiah, A.; Souchet, A.; El-Raghy, T.; Radovic, M.; Sundberg, M.; Barsoum, M.W. Tape Casting, Pressureless Sintering, and Grain Growth in  $Ti_3SiC_2$  Compacts. *J. Am. Ceram. Soc.* **2014**, *87*, 550–556. [[CrossRef](#)]
24. Hu, C.; Sakka, Y.; Tanaka, H.; Nishimura, T.; Grasso, S. Fabrication of Textured  $Nb_4AlC_3$  Ceramic by Slip Casting in a Strong Magnetic Field and Spark Plasma Sintering. *J. Am. Ceram. Soc.* **2011**, *94*, 410–415. [[CrossRef](#)]
25. Hu, C.; Sakka, Y.; Grasso, S.; Suzuki, T.; Tanaka, H. Tailoring  $Ti_3SiC_2$  Ceramic via a Strong Magnetic Field Alignment Method Followed by Spark Plasma Sintering. *J. Am. Ceram. Soc.* **2011**, *94*, 742–748. [[CrossRef](#)]
26. Mishra, M.; Sakka, Y.; Hu, C.; Suzuki, T.S.; Uchikoshi, T.; Besra, L. Electrophoretic Deposition of  $Ti_3SiC_2$  and Texture Development in a Strong Magnetic Field. *J. Am. Ceram. Soc.* **2012**, *95*, 2857–2862. [[CrossRef](#)]
27. Krahrmer, D.M.; Hameed, S.; Sánchez Egea, A.J.; Pérez, D.; Canales, J.; López de Lacalle, L.N. Wear and MnS Layer Adhesion in Uncoated Cutting Tools When Dry and Wet Turning Free-Cutting Steels. *Metals* **2019**, *9*, 556. [[CrossRef](#)]
28. Sánchez Egea, A.J.; Martynenko, V.; Abate, G.; Deferrari, N.; Martinez Krahrmer, D.; López de Lacalle, L.N. Friction capabilities of graphite-based lubricants at room and over 1400 K temperatures. *Int. J. Adv. Manuf. Technol.* **2019**, *102*, 1623–1633. [[CrossRef](#)]
29. Liu, F.; Jia, J.; Yi, G.; Wang, W.; Shan, Y. Mechanical and tribological properties of NiCr– $Al_2O_3$  composites at elevated temperatures. *Tribol. Int.* **2015**, *84*, 1–8. [[CrossRef](#)]
30. Dellacorte, C.; Laskowski, J.A. Tribological Evaluation of PS300: A New Chrome Oxide-Based Solid Lubricant Coating Sliding Against  $Al_2O_3$  from 25 °C to 650 °C. *Tribol. Trans.* **1997**, *40*, 163–167. [[CrossRef](#)]
31. DellaCorte, C.; Edmonds, B.J. NASA PS400: A New High Temperature Solid Lubricant Coating for High Temperature Wear Applications. U.S. Patent 8,753,417, 17 June 2014.
32. Kong, L.; Bi, Q.; Zhu, S.; Yang, J.; Liu, W. Tribological properties of  $ZrO_2$  ( $Y_2O_3$ )–Mo– $BaF_2$ /CaF<sub>2</sub> composites at high temperatures. *Tribol. Int.* **2012**, *45*, 43–49. [[CrossRef](#)]



© 2019 by the authors. Licensee MDPI, Basel, Switzerland. This article is an open access article distributed under the terms and conditions of the Creative Commons Attribution (CC BY) license (<http://creativecommons.org/licenses/by/4.0/>).